Langmuir

ARTICLE

pubs.acs.org/Langmuir

Formation of Nanopore-Spanning Lipid Bilayers through Liposome Fusion

Karthik Kumar,[†] Lucio Isa,[†] Alexander Egner,[‡,§] Roman Schmidt,[‡] Marcus Textor,[†] and Erik Reimhult*[,∥]

[†]Department of Materials, Laboratory for Surface Science and Technology, Swiss Federal Institute of Technology (ETH Zürich), CH-8093 Zürich, Switzerland

[‡]Department of NanoBioPhotonics, Max-Planck Institute, D-37077 Göttingen, Germany

[∥]Department of Nanobiotechnology, University of Natural Resources and Life Sciences (BOKU) Vienna, A-1190 Vienna, Austria

Supporting Information

ABSTRACT: Self-assembly of nanopore-spanning lipid bilayers (npsLBs) paves the way toward chip-based integrated membrane protein biosensing. We present a novel approach to analyze the formation of npsLB at individual nanopores using quantitative analysis of high-resolution microscopy images. From this analysis we derive necessary conditions for the formation of npsLBs on nanopore arrays by liposome fusion and discuss the limitations of the process as a function of nanopore geometry, lipid membrane properties, and surface interaction. Most importantly, applying liposomes with diameters larger than the nanopore is demonstrated to be a necessary but not sufficient condition for npsLB formation. A theoretical model is used to discuss and explain this experimental finding.

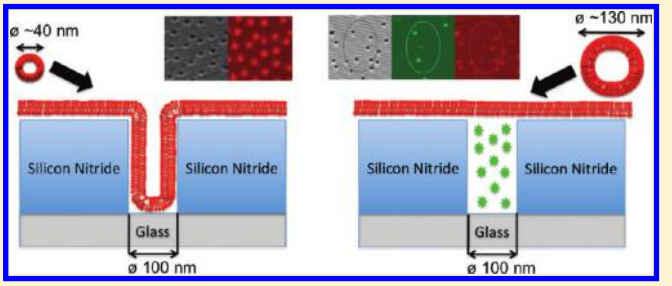

1. INTRODUCTION

Understanding the workings of membrane proteins remains one of the open challenges of present day biology[1] and has a vast impact on drug design and development.[2,3] In vivo studies involve a high degree of complexity, and there is a strong drive toward studying membrane proteins in simpler, controlled model environments. Reconstituted lipid bilayers are good models of real cell membranes and can incorporate delicate membrane proteins in a native environment. This allows membrane protein functions to be directly studied with high-resolution probes under controlled and reproducible conditions.[4] To incorporate membrane proteins with large hydrophilic domains and to enable access to the membrane from both sides, a common approach is to span lipid bilayers across several hundreds of micrometers wide apertures, forming the so-called black lipid membranes (BLM).[5]

BLMs have several drawbacks that have prevented their implementation in biosensing applications, for which robustness and the use of delicate membrane proteins are generally required. Typically, BLMs are spread in the presence of solvents such as decane.[5,6] The large size of the apertures and the solvent remnants cause instabilities in the BLM, in turn causing these sensors to have too-short lifetimes. Moreover, the solvent remnants in the membrane affect the function of membrane proteins, therefore limiting the possibility of studying complex membrane proteins in native environments.[7]

Alternatively, planar membranes bereft of nonpolar solvents can be formed by rupture and fusion of small or large unilamellar liposomes onto solid supports, forming a so-called supported lipid bilayer (SLB) as first reported by Tamm and McConnell.[8] SLBs are increasingly used due to their ease of formation, stability, and adaptability to most common sensing platforms.[9] The improved stability is however achieved at the price of losing the possibility to incorporate many membrane proteins in their native conformation due to steric hindrance and interactions with the solid support.

Combining the ample space for protein incorporation and the small, defined sensor area of BLMs with the robustness, ease of formation, and longevity of supported lipid bilayers would constitute a major leap forward for membrane and membrane protein sensing.[7] Tiefenauer and co-workers demonstrated in 2007 that the lifetimes of solvent-spread BLMs continuously increased as the aperture size was decreased to 200 nm,[10] confirming previously shown long lifetimes of BLMs spread across nanosized pores.[6,11] Höök et al. recently described how solvent-free SLBs preformed at physiological conditions on flat surfaces could be driven by shear flow in microfluidic channels to span nanoholes on another part of the substrate if the pH was increased to 9.5,[12] but it is uncertain whether this method can be applied with large membrane proteins which are pinned from moving at the surface.[13] Naumann and co-workers also recently placed giant vesicles over single nanopores to form nano-BLMs;[14] however, this manual approach does not allow incorporation of membrane proteins by proteoliposomes over large areas of pores.[15]

Received: May 22, 2011
Revised: July 3, 2011
Published: July 12, 2011

A simpler and more desirable process to form nanopore spanning lipid bilayers (npsLB) that could be used for a range of sensor applications would be to exploit vesicle rupture and fusion as is commonly done for SLBs *directly on nanoporous substrates*. However, the direct formation of npsLBs will require a number of necessary conditions to be met in terms of nanostructure geometry and chemistry relative to the chosen proteoliposome properties and SLB assembly conditions which to date have not been consistently explored. A major obstacle in determining the right conditions for npsLB formation has been the difficulty to detect and characterize their formation. The mean-field characterizations typically used for SLBs, such as quartz crystal microbalance with dissipation monitoring (QCM-D)[16] and fluorescence recovery after photobleaching (FRAP),[17] are not sensitive enough to observe SLB conformation over nanostructured surfaces. Electrochemical methods are instead too sensitive, since a defect-free SLB is required over all nanopores in the whole sensing area for detection.[18,19] Finally, mechanical characterization with atomic force microscopy (AFM) of lipid bilayers spanning over nanopores is slow, leading to low statistics, and tip interaction may damage the lipid bilayer.[20]

We present a novel approach towards quantifying the formation of npsLBs by the analysis of high-resolution confocal microscopy images of single nanopores. Several thousands of individual pores were investigated, providing meaningful statistics of the necessary conditions for npsLB formation by liposome fusion directly over high-aspect ratio nanopores etched into silicon nitride, systematically relating the fraction of spanned nanopores to nanopore and vesicle size, lipid composition, and pH. The sensitivity to single nanostructures allowed us for the first time to distinguish between intermediate states of perfectly spanned lipid bilayers and lipid bilayers with nanopore defects. This presents a crucial advantage for further optimization of npsLB formation. The results are discussed in a model for the thermodynamic equilibrium structures and kinetic barriers for conformational changes of membranes at pore nanostructures.

2. EXPERIMENTAL SECTION

2.1. Substrates. Nanostructured substrates (pore sizes: 40, 80, 100, 200, and 500 nm) were produced as previously described by colloidal lithography and etching through 350 nm of plasma-enhanced chemical vapor deposition (PECVD, Plasmalab 80+, Oxford Instruments, U.K.) grown silicon nitride ($n \approx 2.16$) deposited on no. 1 thickness borosilicate microscope glass coverslips.[21] The average nanopore size was determined by the diameter of the colloids. A requirement for the presented analysis was to obtain nanoscale feature separations large enough to allow for the resolution and observation of individual features in a confocal microscope. The pore-to-pore separation can be accurately controlled during the colloidal lithography step by particle self-assembly at liquid−liquid interfaces (SALI).[22] A less accurate but still effective control can be obtained by random adsorption of charged colloids (see Supporting Information for representative images of the substrates).[21,23]

2.2. Buffer. All buffers were made using ultrapure water (Millipore, Zug, Switzerland; $R = 18.2\ \Omega$, TOC < 6 ppb). Tris buffered saline (TBS) was used for all liposome stock solutions: 10 mM tris(hydroxymethyl)-aminomethane (Tris), 150 mM NaCl, and pH 7.4 set by HCl (all chemicals from Fluka, Buchs, Switzerland). Liposome adsorption experiments were performed in TBS with additionally 3 mM $CaCl_2$ added (TBSCa).

2.3. Liposomes (Lipid Vesicles). Fluorescently labeled anionic lipid vesicles were used during the course of these experiments, unless otherwise stated. Vesicles were prepared according to the Barenholz et al.[24] method with the following lipid constituents: 69.8 wt % 1-palmitoyl-2-oleoyl-*sn*-glycero-3-phosphocholine (POPC), 30 wt % 1-palmitoyl-2-oleoyl-*sn*-glycero-3-phospho-L-serine (sodium salt; POPS), and 0.2 wt % 1,2-dioleoyl-*sn*-glycero-3-phosphoethanolamine-*N*-(lissamine rhodamine B sulfonyl) (ammonium salt) (DOPE−RhoB) for negatively charged vesicles and 99.8 wt % POPC and 0.2 wt % DOPE−RhoB for zwitterionic vesicles (Avanti Polar Lipids, Alabaster, AL, USA). For stimulated emission and depletion (STED) measurements, 0.2 wt % DOPE−RhoB was replaced by 0.2 wt % atto-POPE that was synthesized in house (see next section). For demonstrations of fluorescence recovery after photobleaching (FRAP), 0.2 wt % DOPE−RhoB, and 1.8 wt % POPC were replaced by 2 wt % 1-oleoyl-2-[6-[(7-nitro-2−1,3-benzoxadiazol-4-yl)amino] hexanoyl]-*sn*-glycero-3-phosphocholine (NBDPC). Three different sizes of liposomes were prepared by extrusion of the lipid solution through double-stacked 200, 100, and 50 nm polycarbonate filters (Avestin, Mannheim, Germany) according to the protocols of Macdonald et al.,[25] leading to the following diameters of the anionic liposomes, as measured by dynamic light scattering (DLS, Zetasizer NanoZS, Malvern, U.K.) using single Gaussian peak fitting: 200 nm filter, 129.2 ± 17.5 nm; 100 nm filter, 99.4 ± 12.4 nm; 50 nm filter, 74.7 ± 10.6 nm. The vesicles will be referred to in the main text according to their approximate mean diameters: 130, 100, and 75 nm. Note: the standard deviations stated here refer to the standard deviation among the diameters of vesicles from a minimum of three intensity-weighted measurements. Liposomes were suspended in 5 mg/mL stock solutions in TBS and used within 2 weeks from preparation. Solutions were diluted in TBSCa immediately prior to use.

2.4. ATTO-POPE Preparation. To prepare ATTO-POPE, we dissolved 100 μg of NHS ester tagged ATTO dye (ATTO-TEC, Siegen, Germany) in 1 mL of anhydrous, amine-free dimethylformamimide (DMF, Sigma-Aldrich, Buchs, Switzerland) to 0.1 mg/mL. Subsequently we dissolved 170 μg of 1-palmitoyl-2-oleoyl-*sn*-glycero-3-phosphoethanolamine (POPE) in DMF in 340 μL to 0.05 mg/mL. The solutions were mixed and allowed to react for 2 h at room temperature. Finally DMF was evaporated in vacuum and the residue was immediately resuspended in 850 μL $CHCl_3$ to make 0.2 mg/mL of ATTO-POPE with excess POPE solution.

2.5. QCM-D. QCM-D was conducted in batch flow on an E4 QCM-D instrument (Q-Sense, Västra Frölunda, Sweden) where four experiments were conducted simultaneously. 350 nm of silicon nitride were deposited via PECVD on quartz crystals (Q-Sense). Individual crystals were patterned with 40 nm particles, 100 nm particles, and 200 nm amidine latex particles and processed as described elsewhere.[21] All samples were placed in a precleaned UV−ozone cleaner (UV/Ozone Procleaner, Bioforce Nanoscience, Ames, IA, USA) for at least 30 min prior to use. After mounting the crystals in the QCM-D, the crystals were allowed to stabilize in TBSCa to achieve a baseline. Subsequently 0.1 mg/mL of 100 nm negatively charged vesicles (70% POPC, 30% POPS) was introduced at $t = 600$ s in batch flow. Excess vesicles were rinsed away at $t = 1800$ s.

2.6. Confocal Microscopy. Confocal microscopy experiments were conducted in a custom-made open microscopy cell. Before being placed in the microscopy cell, nanopore substrates were thoroughly cleaned by ultrasonication in ethanol and water followed by 30 min of UV−ozone cleaning; substrates were then used within 45 min of removal from the UV chamber. Vesicle solutions were diluted to 0.5 mg/mL in TBSCa and allowed to adsorb directly on the nanopore arrays for at least 15 min, before thoroughly rinsing with TBSCa. Dye encapsulation experiments were conducted using 5(6)-carboxyfluorescein (CF). CF was used as it has a low permeability through planar lipid bilayers. A 1 mg/mL amount of CF was added to TBSCa and filtered to produce a saturated solution of CF−TBSCa. Vesicle solutions were diluted directly into CF−TBSCa as above prior to use. CF experiments were typically conducted within 20 min of initial adsorption. All confocal microscopy experiments were conducted on a Leica SP5 (Leica

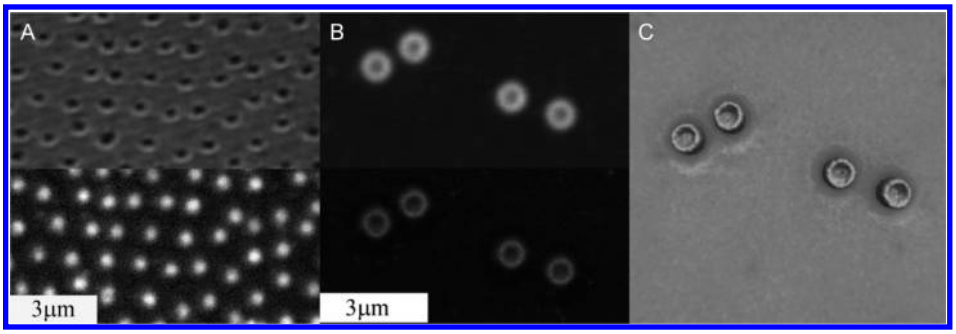

Figure 1. Supported lipid bilayers on nanoporous substrates. (A) Typical corresponding reflection (top) and fluorescence (bottom) CLSM images (200 nm pores obtained by SALI and 130 nm vesicles). In this case, a high fluorescence contrast with respect to the background is observed at the positions of the pores. Note: thresholding makes the fluorescent background surface appear dark. (B) Top, standard CLSM image; bottom, stimulated emission and depletion (STED) image of 500 nm pores with 75 nm vesicles. (C) Snapshot of a 3D image rendered from STED *z*-slices of 500 nm pores with 75 nm vesicles. The fluorescence inside the pore is confined to the walls and the base of the pore. (Full video is available as Supporting Information).

Microsystems, Wetzlar, Germany) inverted setup with an oil immersion 100X N/A 1.4 objective using the 488 and 514 nm lines of the Ar laser and the 561 nm He−Ne laser. Two images were recorded simultaneously: the reflection of the incident laser and the corresponding fluorescence signal of the labeled lipid bilayers. The large difference in refractive index between the silicon nitride ($n \approx 2.16$) and underlying glass substrate ($n \approx 1.52$) and the refractive index of the buffer ($n \approx 1.33$) caused the incident laser light to scatter at the positions of the nanopores. Although all of the recorded images are subject to the diffraction limit of the incident laser line, each nanopore could be accurately located from their respective scattered dark spot since their spacing was larger than the diffraction limit.

2.7. Stimulated Emission and Depletion Imaging. STED microscopy[26,27] was also conducted on the porous silicon nitride. STED images were collected using a Leica TCS STED microscope (Leica) utilizing two pulsed lasers for excitation (diode laser, 635 nm; pulse width < 90 ps) and stimulated emission (Ti:Sa, 750 nm; pulse width ~ 300 ps). Both lasers were running at a repetition rate of 80 MHz and synchronized to each other in order to ensure optimal STED efficiency in the focal plane of the 100X oil immersion objective (NA = 1.4). The resolution of the microscope was routinely checked and found to be between 90 and 100 nm. ATTO-POPE labeled vesicles were used for all STED measurements.

3. RESULTS AND DISCUSSION

3.1. Experimental Results. Formation of SLBs via rupture and fusion of anionic liposomes was first verified both on plain and nanopore-patterned silicon nitride substrates. QCM-D conducted on nanostructured and plain silicon nitride deposited on Au-coated quartz crystals revealed the signature behavior for SLB formation[16,28] on all substrates regardless of nanopore size and density (see Supporting Information for results). Final frequency and dissipation shifts were as expected for this lipid composition: −26 Hz and 0.2×10^{-6}, respectively.[16] FRAP analysis[29] confirmed the presence of an SLB with a mobile fraction of $90.6 \pm 5.2\%$ and a lipid diffusion coefficient of $1.41 \pm 0.31\ \mu m^2/s$. Interestingly, no influence of even up to 5% surface coverage of nanopores on either the SLB assembly kinetics or the final SLB properties could be observed by these techniques.

Figure 1A shows a representative confocal laser scanning (CLS) micrograph of an SLB formed from extruded anionic vesicles with a mean diameter of 130 nm and DOPE−RhoB labeled membranes on a substrate with 200 nm pores. In a typical reflection image such as in Figure 1A, top, each dark circle corresponds to one single pore. Figure 1A, bottom, is the corresponding DOPE−RhoB fluorescence channel. We observe a 1:1 correlation between the openings in the reflection image and the high-fluorescence spots in the fluorescence image. Moreover, the brightness of the features in the bottom image is uniform for all spots. Note: the background top surface in the fluorescence images appears dark due to thresholding but is fluorescent on the level of a supported lipid bilayer. The 1:1 correspondence and uniform brightness was observed for both 200 and 500 nm pores. Although able to resolve single nanopores, conventional CLSM does not have sufficient resolution to resolve the localization of the lipid bilayer in relation to the pore bottom and walls. For this reason STED was employed to image the lipid bilayer arrangement at the nanopores. Figure 1B, top, shows a standard confocal fluorescence image of 500 nm pores and 75 nm vesicles, with Figure 1B, bottom, showing the corresponding STED image (full 3D reconstruction video in Supporting Information; see Figure 1C for snapshot of video). These images prove that the fluorescence signal, and therefore the SLB, follows the contour of the pores. This result, together with the uniform brightness of all fluorescent spots corresponding to nanopores exposed to liposomes, strongly suggests that when the size of our vesicles is smaller than the pore diameter, the liposomes can enter the pore and the planar lipid bilayer therefore forms a continuous SLB following the pore contour.

The situation changes when the size of the nanopore opening is reduced. Parts A−C of Figure 2 show representative CLS micrographs of substrates with 100 nm nanopores exposed to 130 nm DOPE−RhoB labeled liposomes in CF containing buffer; i.e., the average liposome size is larger than the pore diameter. Most positions of nanopores have a corresponding high intensity of fluorescence signal in the DOPE−RhoB channel (Figure 2C), similar to what was observed in Figure 1A. However, in contrast to Figure 1A the remaining pore fraction corresponds to low membrane fluorescence. Interestingly, Figure 2B, showing the buffer label CF channel, yields the inverse image, implying that a pore corresponding to low intensity in the DOPE−RhoB membrane channel has high CF fluorescence intensity. The anticorrelation between the two channels, i.e., high CF correlates with low DOPE−RhoB fluorescence intensity and vice versa, is further illustrated in Figure 2D. The points shown on this plot represent the amount of DOPE−RhoB signal and CF signal coming from each individual nanopore. The points are mainly localized into two

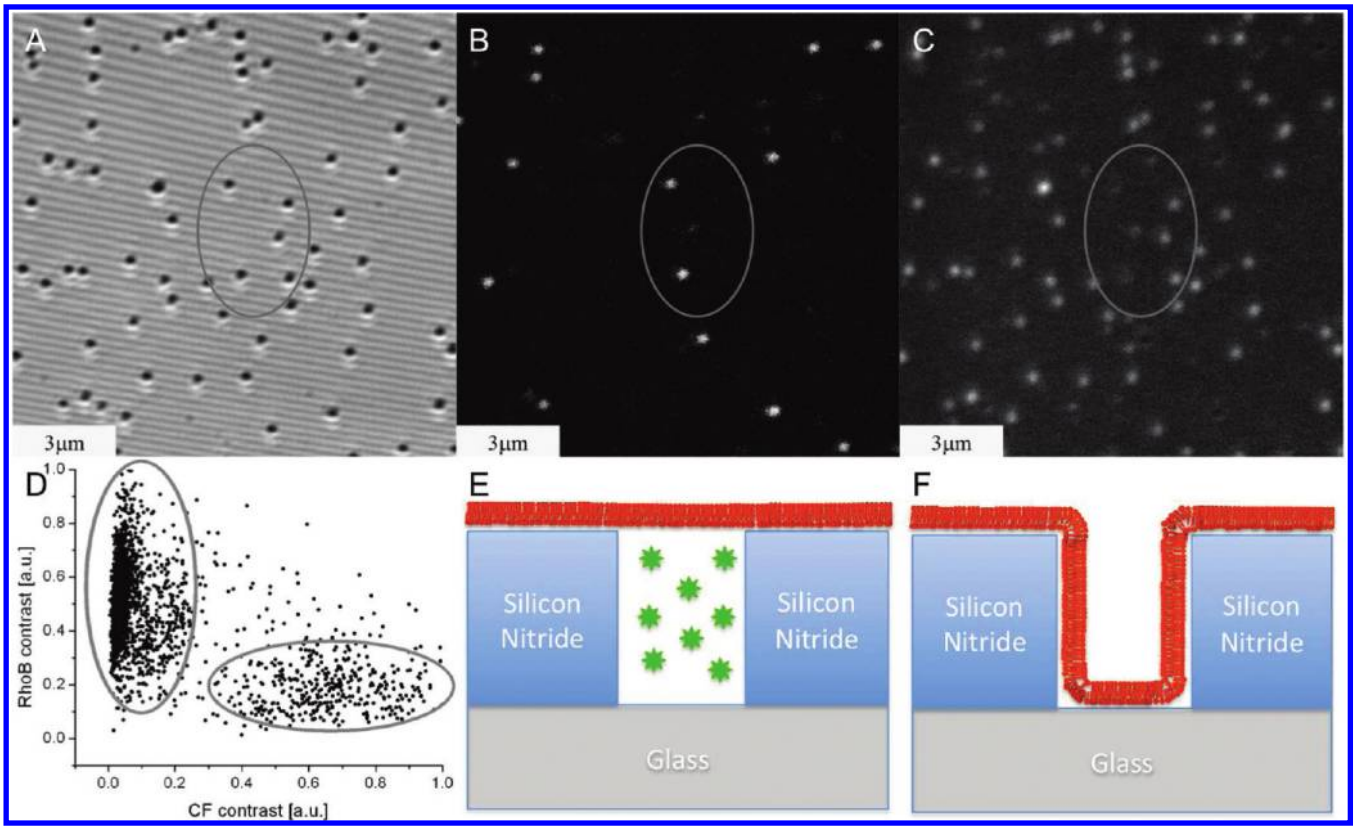

Figure 2. (A) Reflection image of 100 nm nanopores with 130 nm vesicles. Nanopores are distinct, allowing individual identification. (B) Corresponding CF fluorescence image. (C) Corresponding DOPE−RhoB fluorescence image. The highlighted area shows the anticorrelation of CF fluorescence to the DOPE−RhoB signal (high-contrast CF = low-contrast DOPE−RhoB and vice versa). (D) DOPE−RhoB vs CF fluorescence signals. The data points are clustered primarily within two lobes—low CF/high DOPE−RhoB and high CF/low DOPE−RhoB, respectively. (E and F) Schematics explaining the origin of the anticorrelated fluorescence signals. (E) npsLBs encapsulating CF lead to high-CF signal and low-DOPE−RhoB signal. (F) SLBs following the contours of the nanopore lead to high-DOPE−RhoB signal and low-CF signal.

lobes representing nanopores where the signal from only one of the fluorescence channels dominates. Only a low number of outliers are detected with substantial fluorescence in both channels. The interpretation of these results is illustrated in the schematic diagrams provided in Figure 2E,F. A membrane following the contour of the nanopore will not encapsulate any CF dye within the nanopore but will localize more lipid material along the pore walls, which increases the local projected membrane fluorescence signal from the pore as verified above by the STED measurements. Conversely, localization of CF signal to a nanopore implies encapsulation of the dye in the underlying cavity by a spanning lipid bilayer that prevents the dye from diffusing away but also implies that the local membrane (DOPE−RhoB) fluorescence intensity is similar to the one of a planar SLB. Furthermore, due to the strong correlation of a low DOPE−RhoB signal with a high CF signal that unambiguously characterizes a pore spanned by a membrane, we infer that a low DOPE−RhoB signal correlates with the presence of a npsLB. We also attempted direct imaging of the membrane on the small pores using STED. However, the lateral resolution of the STED microscope was limited to ≥90 nm due mainly to optical aberrations on the nanostructured, high-refractive index substrates. This is comparable to the pore diameter (<100 nm), leading to the observation that a free-standing bilayer could not be resolved directly by STED imaging. In fact, in contrast to the data reported in Figure 1B, the small dimensions of the pore make it impossible to distinguish fluorescence localized at the walls from uniform signal across the pore opening from STED images. Therefore the distinction could only be made by looking at the total intensity coming from the individual pores described as follows.

By means of automated algorithms allowing a statistical analysis of a large number of individual nanopores, the amount of fluorescence within the region corresponding to the position of a single nanopore in the reflection image is obtained by the signal contrast from within a nanopore to the background (see Supporting Information) as exemplified by the contrast probability distributions reported in Figure 3A. The peak at high CF signal relating to dye encapsulation and the presence of a npsLB has a broad distribution, indicating that different amounts of CF were encapsulated. From the contrast signal analysis the time evolution of dye encapsulation can also be followed (Figure 3B). The size of the smaller peak as well as its position are continuously decreasing as a function of time between 5 and 180 min, indicating partial leakage and photobleaching. After 180 min, no discernible CF fluorescence was detected under the npsLBs, while the DOPE−RhoB signal still indicated the presence of a npsLB. CF is considered a membrane-impermeable dye. Despite this, both leakage and bleaching of CF have been reported in a similar system with a lipid membrane encapsulating CF within a nanopore[12] and are significantly higher than the leakage observed from a purely liposomal system.[30,31] The difference is likely due to the presence of a layer of water between the lipid membrane and substrate, through which the CF molecules may diffuse and

dx.doi.org/10.1021/la2019132 |*Langmuir* 2011, 27, 10920–10928

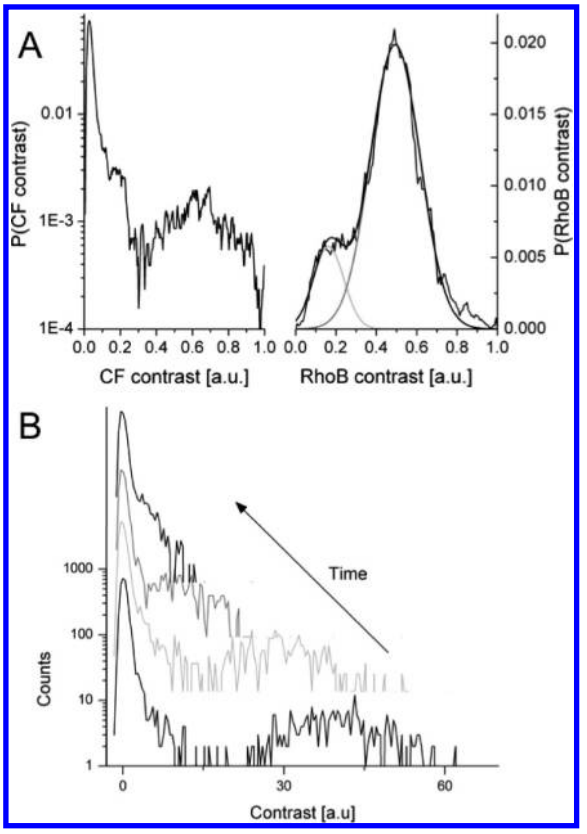

Figure 3. (A) Contrast distributions for CF (thick black line, bottom-left axes) and DOPE−RhoB (thin black line, bottom-right axes) for 130 nm vesicles on 100 nm pores (where, for example, 1E-3 represents 1×10^{-3}). The former is plotted on a linear−logarithmic scale for clarity. Both distributions show two peaks, indicating the existence of two kinds of pores: spanned (CF, high contrast; RhoB, low contrast) and not spanned (CF, low contrast; DOPE−RhoB, high contrast). The DOPE−RhoB distribution is fitted with a linear combination of two Gaussian distributions to quantify the two populations (gray lines). (B) Series depicting the time evolution of the signal from CF encapsulated in pores. The scans are offset for clarity and were taken at 5, 75, 120, and 180 min (bottom to top). CF continuously leaks away as seen from the shift to lower contrast over time of the minority high-contrast fraction of npsLBs.

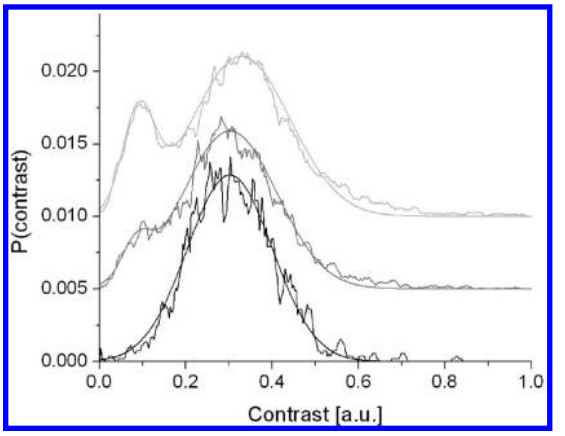

Figure 4. Representative DOPE−RhoB contrast probability distributions of 130, 100, and 75 nm vesicles on 80 nm pores with respective Gaussian fits. The distributions are offset for clarity. The 75 nm vesicles (bottom) show one single peak of high-fluorescence signal within the nanopore. The 100 and 130 nm vesicles (center and top) clearly display two peaks each. For the 130 nm vesicles, the ratio of spanned nanopores to unspanned nanopores increases.

therefore an effectively much larger membrane area where defects can occur is accessible to the dye. Another drawback of using CF to check for encapsulation is the low number of encapsulated CF molecules per nanopore. However, the continuous and slow rate of single-nanopore CF signal loss is proof of the long-term stability of the spanning bilayers. The time for loss of the encapsulated CF signal is, e.g., 3 times longer than reported for CF encapsulated in similar nanopores by shear-flow membrane spreading.[12]

The described anticorrelation between the CF and DOPE−RhoB signals allows us to rely on using only one dye, which is preferred in order to avoid cross-talk, to investigate the presence of npsLB. Analysis based on using only the membrane dye RhoB yields sharper contrast distribution for npsLB events due to lower variability in the encapsulated dye and less time dependence of the contrast, which for DOPE−RhoB is not affected by leakage and nonuniform bleaching. The following analysis therefore relates to the DOPE−RhoB signal.

Figure 4 shows a typical set of results reporting the DOPE−RhoB contrast distributions obtained by varying the size of vesicles (75, 100, and 130 nm, respectively) and keeping the size of the nanopores constant, in this case 80 nm. For clarity, the values of the contrast have been normalized between the minimum and maximum contrasts in the raw images and each curve has been obtained by analyzing several thousands of pores. The curve for 75 nm vesicles exhibits a single, high-fluorescence peak indicating that no npsLBs were observed. The 100 nm vesicles on the other hand display a clear dual population of peaks—a large number of nanopores with high-fluorescence signal, with a small number of pores with low-fluorescence signal indicating the presence of some npSLBs. The number of membrane-spanned pores with low fluorescence increases when 130 nm vesicles are used instead of 100 nm vesicles. The contrast distribution for each vesicle size was fitted using two Gaussians (shown in Figure 3A), and the percentage of spanning pores was calculated as the ratio of the areas of the two Gaussians.

Such analysis was extended to the whole matrix of pore/vesicle sizes available for our study. The resulting percentages of membrane-spanned pores as a function of nanopore diameter are shown in Figure 5. The error bars range between the minimum and maximum spanning percentage achieved repeating the experiments with different vesicle batches and substrates for a given nanopore size. The fraction of spanned nanopores shows a strong dependence on the vesicle size to pore diameter. Pores that are 200 or 500 nm in diameter are never spanned by any size of vesicles tested. As the pore size is decreased, formation of npsLB is observed with the onset of spanning occurring roughly at a nanopore size corresponding to the average vesicle diameter. The fraction of npsLBs then increases with the difference between vesicle and pore diameter, but seems to saturate at an average close to 15% for both 100 and 130 nm vesicles. Importantly, this saturation level seems to be reached already at a size difference of roughly 30%, after which a further increase in relative vesicle size has no significant influence on the npsLB fraction. The highest observed npsLB fraction of 24% was observed for 130 nm vesicles over 100 nm pores. The appearance of an upper limit to the fraction of nanopores that can be spanned by a lipid membrane formed by liposome fusion is a new and somewhat surprising finding. We discuss this finding in the following section in terms of the free energy contributions from

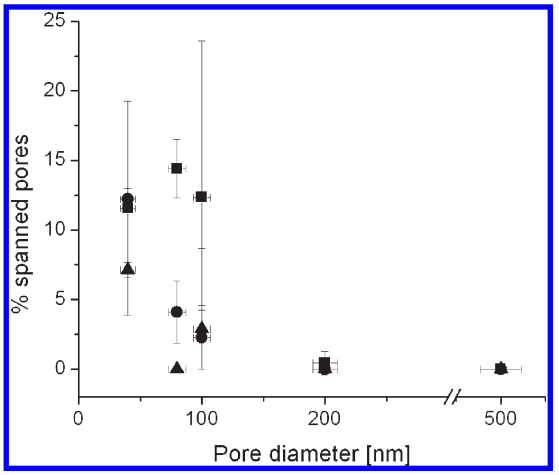

Figure 5. Plot of percentage of spanned pores versus pore size. Response curves for each size of vesicle are plotted against the different diameters of nanopores: ■, 130 nm vesicles; ●, 100 nm vesicles; ▲, 75 nm vesicles. The vertical error bars range between the minimum and maximum spanning percentage achieved repeating the experiments with different vesicle batches and substrates for a given nanopore size. The horizontal error bars are the standard deviations in the diameters of the particles used. Vesicles do not span pores with diameters > 100 nm. Spanning occurs only for nanopores with a diameter ≤ 100 nm. A larger vesicle size to pore diameter leads to a higher fraction of npsLBs. The maximum obtained npsLB fraction was 24%.

membrane bending and adhesion that shapes the membrane conformation around a nanopore.

3.2. Theoretical Considerations. The geometry of a nanopore is sketched in Figure 6A. The curvatures and distances are not to scale. *a* refers to the radius of curvature of the nanopore edge determined to be <10 nm by scanning electron microscopy (SEM), *c* refers to the radius of the curvature of the nanopore opening, $R = c - a$ refers to the internal radius of the nanopore given by the lithographically defined pore size, and *h* refers to the height of the nanopore. The POPC and POPS lipids used in this work both have a shape factor close to 1,[32,33] meaning that a membrane formed from these lipids will have insignificant intrinsic curvature and prefer a planar conformation; any bending imposed to the bilayer causes therefore an energy penalty for the system. The bending energy of such an SLB over a curved surface of area *S* can be derived from the Helfrich harmonic approximation:[34,35]

$$E_b = \oint_S e_b \, dA \tag{1}$$

where

$$e_b = \frac{1}{2}k_b(\kappa_1 + \kappa_2 - 2c_0)^2 + \aleph\kappa_1\kappa_2 \tag{2}$$

k_b is the bending modulus, κ_1, κ_2 are the principal curvatures of the lipid bilayer segment, c_0 is the spontaneous curvature, and $\aleph$ is the saddle splay modulus. Seifert[36] quoted a typical bending modulus $k_b = 10^{-19}$ J. The spontaneous curvature c_0 of a flat SLB with our chosen lipid composition can be taken to be 0, while the saddle splay modulus $\aleph$ is neglected because topological changes of the SLB over a single edge are not considered, reducing (2) to $e_b = (1/2)k_b(\kappa_1 + \kappa_2)$. For the current purpose, the principal radius κ_1, referring to the lipid bilayer segment stretching/compression across the nanopore edge, is taken to be constant as it follows

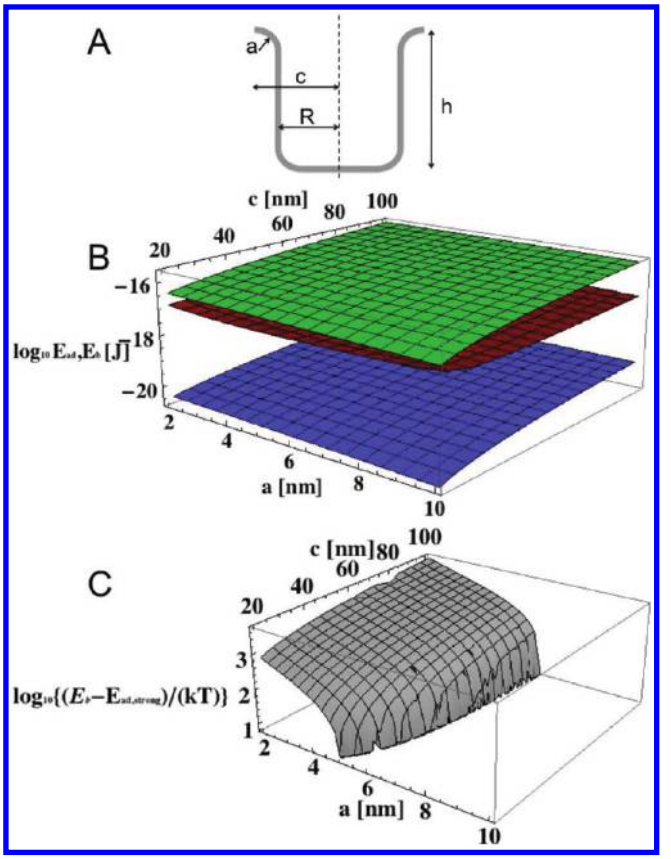

Figure 6. Results of theoretical calculations for the formation of nanopore-spanning lipid bilayers over a nanopore. (A) Sketch of a single nanopore: *a*, radius of curvature of the nanopore edge; *c*, radius of nanopore opening; *R*, internal radius of the nanopore; *h*, height of the nanopore. (B) Energy landscapes for the bending energy E_b and adhesion energy E_{ad} for a SLB adsorbed in a nanopore for a range of nanopore dimensions. The red surface represents the bending energy landscape for a SLB following the contours of the nanopore, the green surface represents the adhesion energy for a strongly adhering SLB, and the blue surface represents the adhesion energy for a weakly adhering SLB. (C) Difference between bending energy of a membrane over the nanopore edge, $E_{b,edge}$, and the adhesion energy of the membrane to the edge, $E_{ad,edge,strong}$. Only values where $E_{b,edge} > E_{ad,edge,strong}$ favoring formation of a npsLB are displayed.

the curvature of the nanopore opening ($\kappa_1 = 1/a$). The second principal radius κ_2, referring to the stretching/compression along the edge of the opening of the nanopore, is instead not constant and is a function of both the nanopore curvature and nanopore edge curvature. The same assumptions and considerations are applicable to the bottom of our nanopores (Figure 6A). The parametrization of these curved surfaces are derived in the Supporting Information. In addition to bending at the nanopore edge, the bending induced by the adhesion of the bilayer onto the inner walls of a cylindrical pore has to be accounted for; in this case the inverse pore radius $1/R$ is the only principal curvature radius. The total energy penalty stemming from bending at and within a nanopore is thus given by summing up the contributions from each curved surface, $E_{b,total} = E_{b,edge} + E_{b,bottom,edge} + E_{b,wall}$.

The adhesion energy between the membrane and substrate can be written as

$$E_{ad} = k_{ad}A_{pore} \tag{3}$$

dx.doi.org/10.1021/la2019132 |*Langmuir* 2011, 27, 10920–10928

where k_{ad} is the adhesion energy per unit area for a given lipid system/surface pair and A_{pore} is the area of contact. Experimental values for k_{ad} vary between 10^{-21} and 10^{-25} J nm^{-2} for strongly to weakly adhering SLBs as measured by a variety of methods such as the surface force apparatus, optical microscopy, and reflection interference contrast microscopy.[34,36] In the case of our nanopores, the contact area is approximately the internal area of a cylindrical pore with radius R and height h including only the bottom face, the area of the nanopore edge, and the area joining the walls of the nanopore and the bottom face, as parametrized and calculated in the Supporting Information.

To understand the prevailing energy contribution which will determine the equilibrium configuration of the lipid membrane for various pore geometries, E_b and E_a are plotted as a function of a and c in Figure 6B. The minimum value for a of 2 nm reflects the theoretical minimum possible bending radius of a lipid bilayer segment around a high curvature edge given the size of a lipid, while the maximum value is the upper bound to the radius of curvature given by the resolution of SEM images of the edge. The values of c represent the range of diameters for which npsLBs were detected in this study and a nanopore depth h of 350 nm was assumed, corresponding to the deposited silicon nitride. The values of E_b (red) lie between the adhesion energies for strongly (green) and weakly (blue) adhering lipid bilayers. Thus, in first approximation, a strongly adhering SLB for which $E_b < E_a$ will bend and follow the contour of the nanopore. The expected outcome, however, depends dramatically on the not well-known value of k_{ad}. A high adhesion energy between vesicles and the underlying surface is required for the formation of SLBs through liposome fusion, in particular for anionic membranes formed in the presence of Ca^{2+}.[37] This implies that the k_{ad} value for our system is likely to be close to the maximum reported values, yielding that npsLBs are not likely to occur according to the presented minimum energy arguments.

The data presented in Figure 5 can now be assessed according to the insights provided by these calculations. Vesicles smaller than the nanopore openings will only form SLBs following the contours of nanopore arrays by diffusing into them. For the cases with vesicles larger than the nanopore openings, the majority of the pores show no evidence of spanning, in agreement with the results of the thermodynamic equilibrium analysis. However, a substantial fraction of npsLBs is also found, which according to the above analysis should not occur. This implies that a second mechanism must be at play for the formation of npsLBs and that the equilibrium analysis is not sufficient to explain the experimental results.

Vesicles are known to adsorb to silicon nitride and rupture upon reaching a critical surface concentration (~30%), forming SLB patches on the surface.[16,38] Each SLB patch will fuse with other patches across the surface upon addition of lipid material from incoming vesicles. A continuous addition of lipid material from the bulk thus expands the merging patch sizes by diffusion of lipids along the surface to form a fully connected lipid bilayer as liposomes from the bulk solution adsorb and rupture at the edge of a membrane patch. When the lipid bilayer front reaches a topographical feature on the surface, the membrane will flow over or into them, as has been observed previously for low aspect ratio features with low curvature[39−41] and for shear-driven SLBs,[12] but the probability of which will occur depends on the kinetic barrier to the formation of a contour-following SLB. The incremental bending energy as the membrane moves over the nanopore edge must be sufficiently greater than the incremental adhesion energy. The energy landscapes for these contributions taking only the barrier zone of the nanopore edge into account can be similarly derived and plotted as a function of nanopore size, such as for Figure 6B (see Supporting Information). The resulting energy barrier height obtained by subtracting $E_{ad,edge}$ from $E_{b,edge}$ normalized by kT is plotted in Figure 6C. Only the highest adhesion energy found in literature was chosen, reflecting the case most unfavorable to the formation of npsLB. $E_{b,edge} - E_{ad,edge} \gg kT$ for small a, but is seen to drop below 0 for 4 nm < a < 6 nm, while only a weak dependence on nanopore radius is observed. Thus, for very small a it can be predicted that the moving SLB front is unlikely to enter the nanopore and adhere to its walls even if the highest reported adhesion constant is assumed. Note that even if the membrane at a high-curvature edge adopts a low-curvature shape around that edge, this can only happen by losing the contact to the surface and thus reducing the adhesion energy to zero while still suffering a significant penalty for the lower bending but over a large area. It can be observed that for 4 nm < a < 6 nm, the rate of change of $(E_{b,edge} - E_{ad,edge})/kT$ is very high, and therefore small geometrical variations are responsible for favoring either an npsLB or a contour following SLB.

Thus, from a first theoretical analysis of the SLB around a nanopore, it can be seen that two factors determine the formation of npsLBs, namely, k_{ad} and the geometry of the nanopores defined by a and c. The conditions which favor the formation of npsLBs are low k_{ad}, a, and c, where c plays a less important role. In agreement with the experimental observation of both npsLB and contour following SLB, it was shown that, for the relevant parameter range, the contour following SLB is the minimum energy state but that the energy barrier to reach the minimum can vary to favor each of the conformations within the experimental parameter range and sample polydispersity. In light of this, two approaches to promote npsLB formation through reduction of the adhesion energy respectively during and after liposome adsorption were attempted. The first approach was based on the adsorption of zwitterionic POPC liposomes in Ca^{2+}-free buffer with lower surface affinity,[16] which resulted in more defective SLBs but percentages of npsLB similar to those for anionic liposomes with Ca^{2+} for 100 (3 ± 1%) and 140 nm (10 ± 1%) vesicles on 100 nm pores. While the adhesion energy and thus vesicle rupture and fusion were different for anionic and zwitterionic vesicles, the kinetics of SLB spreading are essentially the same,[16] suggesting that the adhesion energies of the anionic and zwitterionic lipid bilayers are in the same order of magnitude. This leads to equal, low fractions of npsLB.

The second approach to reduce membrane surface adhesion on silica surfaces, introduced by Cremer and Boxer[17] and recently used to favor formation of npsLBs for membranes driven across nanoporous substrates,[12] is changing the pH of the buffer. We therefore adsorbed vesicles at pH 7.4, after which the buffer was changed to pH 9.5 to observe whether a release of the membrane adhering to the inside of the pore would occur to form a npsLB. However, even after waiting for prolonged periods of time (180 min), no increase in npsLB fraction was observed (5 ± 1% of spanned pores with 100 nm vesicles and 12 ± 1% of spanned pores from 130 nm vesicles exposed to 100 nm nanopores). It was concluded that, as predicted above, already formed contour-following SLBs cannot be converted into npsLBs, as this would both require the npsLB to be the equilibrium conformation and that a large energy barrier due to giving up favorable adhesion energy from the low-curvature nanopore walls is overcome.

A consequence of our analysis is that a npsLB is never obtained unless the membrane is originally formed over the pore and stays

as such. A lipid bilayer prepositioned above a nanopore occurs in the experiment when vesicles larger than the nanopore either sit on top of the pore or in very close proximity to a nanopore and extend over it. A vesicle positioned over a pore will already have the membrane correctly positioned to form a sealing npsLB when rupturing by fusing to a spreading SLB, which then cannot enter the pore. This mechanism is inherently stochastic, relying on the probability of vesicles to randomly adhere onto nanopore openings on the substrate, and therefore this could also explain the fact that only a fraction of the nanopores can be spanned. The frequency of occurrence of a vesicle positioning itself over a pore depends thus on vesicle size. Adsorption over a pore is additionally only possible when the local vesicle area coverage does not partially block the pore opening. Therefore, once the necessary conditions for spanning through liposome fusion are met, i.e. the vesicle diameter is larger than the pore diameter, the spanned pore fraction is only weakly dependent on the vesicle-to-pore size ratio leading to the observed saturation value for the fraction of spanned pores.[17] The necessity of a vesicle to be already positioned on top of a nanopore in order to lead to the formation of a spanning membrane is also supported by the fact that the maximum achieved fraction of spanned pores is close to the critical surface coverage necessary to cause vesicle rupture and bilayer formation (∼30%). At the critical coverage, we expect roughly 30% of the pores to be occupied by a vesicle, leading to a similar fraction of pore-spanning bilayers when these vesicles rupture and fuse with bilayer forming in the immediate vicinity. The fact that the measured fractions are somewhat lower can be due to the fact that the probability of a vesicle adsorbing on top of a pore opening is likely smaller than on the silicon nitride surface since the contact area with the substrate is reduced. Finally, as described in the Experimental Section the vesicles exist with a quite broad distribution of sizes also after extrusion. This certainly causes a minor lowering in the spanned fraction due to the tail of smaller vesicles that are present also in, e.g., the 130 nm vesicle samples. The correction is expected to be minor as, e.g., the 130 nm vesicle sample only ∼5% of the total population of vesicles is estimated to be smaller than 100 nm in diameter on the basis of the DLS analysis.

4. CONCLUSIONS

In summary, to promote the formation of solvent-free npsLBs by the preferred method of liposome rupture and fusion, a series of necessary criteria have to be met, including a minimum liposome to pore diameter ratio, high-curvature pore edges, and a sufficiently strong liposome−substrate adhesion energy to promote SLB formation through the right choice of substrate chemistry, lipid and buffer compositions. This was shown and quantified by detailed image analysis of high-resolution optical micrographs, which for the first time provided statistics of membrane conformation also on small nanostructures.

The detailed statistics showed that the *necessary* requirements put forth above are not *sufficient* to promote npsLB formation over all pores on a nanoporous array sensor substrate. Even in the best-case scenario, where these parameters are optimized to favor the npsLB structure over an SLB following the nanopore contour, the kinetics of the SLB formation or polydispersity of current sample manufacturing technology will lead to only a fraction (for us maximum ∼ 1/4) of the pores being spanned.

How would it then be possible to form a solvent-free npsLB by direct liposome fusion over an entire nanopore array? The presented work shifts the focus from the energetic equilibrium of membrane conformation over the nanostructures to the kinetics of its formation; providing a sufficient barrier that opposes a membrane entering a pore while forming constitutes therefore an additional requirement. Several future solutions can be envisaged, e.g., to prevent the spreading SLB patches from entering pores smaller than the adsorbing liposomes by functionalizing selectively the pore walls with liposome repelling polymers such as poly(ethylene glycole) (PEG) brushes. In more advanced approaches, liposomes could be tailored to bind selectively only on top of the openings, followed by a second step where a lipid bilayer is either formed on the substrate around the pores or is driven there and then allowed to fuse with the preplaced liposomes. By means of such preplacement of vesicles we can also envisage the possibility of localizing membrane proteins primarily to the nanostructure sensor elements.

■ ASSOCIATED CONTENT

Supporting Information. Table listing amidine latex polystyrene particle specifications, text describing SEM images of 200 nm pores, QCM-D analysis, quantitative image analysis, and derived energy landscapes, and figures showing SEM images of 200 nm pores in silicon nitride and FIB sectioned 200 nm pores, and QCM-D graph of negatively charged vesicles (pdf) and video showing supported lipid bilayer following the walls of the nanopores. This material is available free of charge via the Internet at http://pubs.acs.org.

■ AUTHOR INFORMATION

Corresponding Author

*Tel.: +431476542230. Fax: +4314789112. E-mail: erik.reimhult@boku.ac.at.

Present Addresses

[§]Department of Optical Nanoscopy, Laser Laboratory Göttingen e.V., D-37077 Göttingen, Germany.

■ ACKNOWLEDGMENT

We thank the FIRST Center for Micro- and Nanoscience and the Light Microscopy Centre at the ETH Zurich and the Center for Microscopy and Image Analysis at the University of Zurich for the use of these facilities and the support provided. EU-FP7-NMP-ASMENA, the Agency for Science, Technology and Research (Singapore), and the ETH Zurich are acknowledged for financial support.

■ REFERENCES

(1) Rosenbaum, D. M.; Rasmussen, S. G. F.; Kobilka, B. K. The structure and function of G-protein-coupled receptors. *Nature* **2009**, *459* (7245), 356–363.

(2) Arinaminpathy, Y.; Khurana, E.; Engelman, D.; Gerstein, M. Computational analysis of membrane proteins: the largest class of drug targets. *Drug Discovery Today* **2009**, *14* (23−24), 1130–1135.

(3) Fang, Y.; Hong, Y.; Webb, B.; Lahiri, J. Applications of biomembranes in drug discovery. *MRS Bull.* **2006**, *31* (7), 541–545.

(4) Cooper, M. Advances in membrane receptor screening and analysis. *J. Mol. Recognit.* **2004**, *17* (4), 286–315.

(5) Mueller, P.; Wescott, W.; Rudin, D.; Tien, H. Methods for formation of single bimolecular lipid membranes in aqueous solution. *J. Phys. Chem.* **1963**, *67* (2), 534–535.

(6) Romer, W.; Steinem, C. Impedance analysis and single-channel recordings on nano-black lipid membranes based on porous alumina. *Biophys. J.* **2004**, *86* (2), 955–965.
(7) Reimhult, E.; Kumar, K. Membrane biosensor platforms using nano- and microporous supports. *Trends Biotechnol.* **2008**, *26* (2), 82–89.
(8) Tamm, L.; McConnell, H. Supported phospholipid bilayers. *Biophys. J.* **1985**, *47*, 105–113.
(9) Castellana, E. T.; Cremer, P. S. Solid supported lipid bilayers: From biophysical studies to sensor design. *Surf. Sci. Rep.* **2006**, *61* (10), 429–444.
(10) Han, X.; Studer, A.; Sehr, H.; Geissbuehler, I.; Di Berardino, M.; Winkler, F. K.; Tiefenauer, L. X. Nanopore arrays for stable and functional free-standing lipid bilayers. *Adv. Mater.* **2007**, *19* (24), 4466–4470.
(11) Kepplinger, C.; Hoefer, I.; Steinem, C. Impedance analysis of valinomycin activity in nano-BLMs. *Chem. Phys. Lipids* **2009**, *160* (2), 109–113.
(12) Jönsson, P.; Jonsson, M.; Höök, F. Sealing of submicrometer wells by a shear-driven lipid bilayer. *Nano Lett.* **2010**, *10*, 1900–1906.
(13) Jönsson, P.; Gunnarsson, A.; Höök, F. Accumulation and separation of membrane-bound proteins using hydrodynamic forces. *Anal. Chem.* **2010**, *83*, 604–611.
(14) Kresak, S.; Hianik, T.; Naumann, R. L. C. Giga-seal solvent-free bilayer lipid membranes: From single nanopores to nanopore arrays. *Soft Matter* **2009**, *5* (20), 4021–4032.
(15) Schmitt, E. K.; Nurnabi, M.; Bushby, R. J.; Steinem, C. Electrically insulating pore-suspending membranes on highly ordered porous alumina obtained from vesicle spreading. *Soft Matter* **2008**, *4* (2), 250–253.
(16) Reimhult, E.; Hook, F.; Kasemo, B. Intact vesicle adsorption and supported biomembrane formation from vesicles in solution: Influence of surface chemistry, vesicle size, temperature, and osmotic pressure. *Langmuir* **2003**, *19*, 1681–1691.
(17) Cremer, P.; Boxer, S. Formation and spreading of lipid bilayers on planar glass supports. *J. Phys. Chem. B* **1999**, *103* (13), 2554–2559.
(18) Naumann, R.; Schiller, S.; Giess, F.; Grohe, B. Tethered lipid bilayers on ultraflat gold surfaces. *Langmuir* **2003**, *19*, 5435–5443.
(19) Schmitt, E. K.; Weichbrodt, C.; Steinem, C. Impedance analysis of gramicidin D in pore-suspending membranes. *Soft Matter* **2009**, *5* (17), 3347–3353.
(20) Mey, I.; Stephan, M.; Schmitt, E. K.; Mueller, M. M.; Ben Amar, M.; Steinem, C.; Janshoff, A. Local membrane mechanics of pore-spanning bilayers. *J. Am. Chem. Soc.* **2009**, *131*, 7031–7039.
(21) Reimhult, E.; Kumar, K.; Knoll, W. Fabrication of nanoporous silicon nitride and silicon oxide films of controlled size and porosity for combined electrochemical and waveguide measurements. *Nanotechnology* **2007**, *18* (27), 275303.
(22) Isa, L.; Kumar, K.; Müller, M.; Grolig, J.; Textor, M.; Reimhult, E. Particle lithography from colloidal self-assembly at liquid−liquid interfaces (SALI). *ACS Nano* **2010**, *4*, 5665–5670.
(23) Hanarp, P.; Sutherland, D.; Gold, J.; Kasemo, B. Control of nanoparticle film structure for colloidal lithography. *Colloids Surf., A* **2003**, *214* (1−3), 23–36.
(24) Barenholz, Y.; Gibbes, D.; Litman, B.; Goll, J. A simple method for the preparation of homogeneous phospholipid vesicles. *Biochemistry* **1977**, *16*, 2806–2810.
(25) MacDonald, R.; MacDonald, R.; Menco, B.; Takeshita, K.; Subbarao, N.; Hu, L. Small-volume extrusion apparatus for preparation of large, unilamellar vesicles. *Biochim. Biophys. Acta* **1991**, *1061*, 297–303.
(26) Hell, S. Toward fluorescence nanoscopy. *Nat. Biotechnol.* **2003**, *21* (11), 1347–1355.
(27) Hell, S.; Wichmann, J. Breaking the diffraction resolution limit by stimulated emission: Stimulated-emission-depletion fluorescence microscopy. *Opt. Lett.* **1994**, *19* (11), 780–782.
(28) Keller, C.; Kasemo, B. Surface specific kinetics of lipid vesicle adsorption measured with a quartz crystal microbalance. *Biophys. J.* **1998**, *75* (3), 1397–1402.
(29) Jönsson, P.; Jonsson, M. P.; Tegenfeldt, J. O.; Höök, F. A method improving the accuracy of fluorescence recovery after photobleaching analysis. *Biophys. J.* **2008**, *95* (11), 5334–5348.
(30) de la Maza, A.; Parra, J. L. Solubilizing effects caused by the nonionic surfactant dodecylmaltoside in phosphatidylcholine liposomes. *Biophys. J.* **1997**, *72* (4), 1668–1675.
(31) Ferdani, R.; Li, R.; Pajewski, R.; Pajewska, J.; Winter, R. K.; Gokel, G. W. Transport of chloride and carboxyfluorescein through phospholipid vesicle membranes by heptapeptide amphiphiles. *Org. Biomol. Chem.* **2007**, *5* (15), 2423–2432.
(32) Dickey, A.; Faller, R. Examining the contributions of lipid shape and headgroup charge on bilayer behavior. *Biophys. J.* **2008**, *95* 2636–2646.
(33) Mashaghi, A.; Swann, M.; Popplewell, J.; Textor, M.; Reimhult, E. Optical anisotropy of supported lipid structures probed by waveguide spectroscopy and its application to study of supported lipid bilayer formation kinetics. *Anal. Chem.* **2008**, *80*, 3666–3676.
(34) Deserno, M.; Gelbart, W. Adhesion and wrapping in colloid-vesicle complexes. *J. Phys. Chem. B* **2002**, *106*, 5543–5552.
(35) Zhong-Can, O.; Helfrich, W. Bending energy of vesicle membranes: General expressions for the first, second, and third variation of the shape energy and applications to spheres and cylinders. *Phys. Rev. A* **1989**, *39* (10), 5280–5288.
(36) Seifert, U. Configurations of fluid membranes and vesicles. *Adv. Phys.* **1997**, *46* (1), 13–137.
(37) Khan, T.; Grandin, H.; Mashaghi, A.; Textor, M.; Reimhult, E.; Reviakine, I. Lipid redistribution in phosphatidylserine-containing vesicles adsorbing on titania. *Biointerphases* **2008**, *3* (2), FA90–FA95.
(38) Reimhult, E.; Zäch, M.; Höök, F.; Kasemo, B. A multitechnique study of liposome adsorption on Au and lipid bilayer formation on SiO_2. *Langmuir* **2006**, *22*, 3313–3319.
(39) Furukawa, K.; Sumitomo, K.; Nakashima, H.; Kashimura, Y.; Torimitsu, K. Supported lipid bilayer self-spreading on a nanostructured silicon surface. *Langmuir* **2007**, *23*, 367–371.
(40) Jonsson, M.; Jönsson, P.; Dahlin, A.; Höök, F. Supported lipid bilayer formation and lipid-membrane-mediated biorecognition reactions studied with a new nanoplasmonic sensor template. *Nano Lett.* **2007**, *7*, 3462–3468.
(41) Roiter, Y.; Ornatska, M.; Rammohan, A. R.; Balakrishnan, J.; Heine, D. R.; Minko, S. Interaction of nanoparticles with lipid membrane. *Nano Lett.* **2008**, *8*, 941–944.